MATERIALS SCIENCE

Damage-resistant and body-temperature shape memory skin-mimic elastomer for biomedical applications

Jiaxin Shi[1], Fei Xia[2], Qingchao Tu[2], Chen Wang[2], Zhiqi Wang[1], Bo Li[1], Baohua Guo[1], Chong Qiu[2]*, Jun Xu[1]*

The integration of high strength, super toughness, damage resistance, body-temperature shape memory, and biosafety into a single skin-mimic material system has been a notable challenge in the realm of material science and biomedical applications. In this study, "Lego-like" polyurethane (PU) was selected to amalgamate multiple properties through the design of multilevel structures. By comprehensively designing the chemical and sequence structures of blocks, coordinating weak/strong hydrogen bonds, and achieving rational microphase separation and crystallization, an elastomer was obtained with an exceptional true tensile strength of 1.42 gigapascal, a high fracture energy of 384.7 ± 18.9 kJ/m^2, and a skin-like nonlinear mechanoresponse. The coordination of crystallization and physical cross-linking also guaranteed excellent body-temperature shape memory properties, which are applicable in 4D printing. Moreover, the obtained elastomer is biosafe and has the potential to promote cell proliferation and DNA repair, which will find wide applications in the biomedical field including minimally invasive surgery.

INTRODUCTION

As a family of candidate materials, elastomers have played a notable role in biomedical applications due to their mechanical properties similar to those of biological soft tissues (*1*–*4*), including flexibility, elasticity, and toughness. However, during evolution for hundreds of millions of years, creatures in nature have attained a high degree of rationality in numerous aspects, which has led to the current situation that the performance of synthetic elastomers is unsatisfactory compared with soft tissues. Minimally invasive surgery has developed rapidly in recent years, and its inevitable demand for shape memory polymers has also imposed new requirements on biomedical elastomers (*5*–*7*). Therefore, there is an urgent need for a novel molecular design of materials that combines shape memory property and mechanical properties similar to or even surpassing those of biological soft tissues into one synthetic elastomer.

Biological soft tissues, such as skin, exhibit strain-stiffening mechanical behavior (*8*). Specifically, the initially soft and compliant skin has the capacity to rapidly stiffen upon substantial deformation. This leads to an increase in elastic modulus by several orders of magnitude, thereby effectively preventing injury. In addition, the skin is highly strong and exhibits remarkable resistance to tear and puncture. These properties endow it with the ability to provide protection and endure in harsh environments. The special mechanical property originates from the intertwined structure of elastin and collagen (Fig. 1A), in which the flexible elastin unfolds under the applied force at a small strain, while the rigid collagen backbones are stretched at a higher strain. Inspired by the structure of the skin, distinct networks with different rigidities have been integrated to mimic strain-stiffening properties by the progressive response to strain, such as bottle-brush elastomers (*9*) and hybrid crosslinked networks (*10*–*12*).

Despite substantial progress, most of the reported skin-like elastomers usually have limitations that significantly hamper their further applications. These elastomers usually involved weak crosslinks to ensure their intrinsic softness, nevertheless leading to poor strength and tear resistance. Besides, shape memory properties are often difficult to coexist with excellent mechanical properties. The shape memory response of medical materials should ideally occur at body temperature, which needs precisely controlling the glass transition temperature or the crystal melting point (*13*, *14*). Biocompatibility and biodegradability are also essential for medical materials. Therefore, resolving the aforementioned issues requires the balance of numerous contradictions, such as strong/weak, rigid/flexible, and crystalline/amorphous structures, which undoubtedly represents a notably challenge.

Recently, the "Lego"-like modular designability of polyurethane (PU) has attracted extensive attention. The hierarchical structures can be regulated via adopting soft and hard segments to achieve the target performance (*15*–*25*). Through block design, it is expected that the strain-induced crystallization required for strain-stiffening, the coupling of strong and weak hydrogen bonds necessary for damage resistance, the crystallization control needed for shape memory, and the hydrolyzable groups essential for biodegradation can be integrated into one elastomer, thereby bridging the abovementioned gaps.

In this work, we coordinated the interplay of hydrogen bonds, microphase separation, and crystallization through block design, thereby enabling the obtained PU elastomer with J-shaped mechanical behavior, ultra-high strength, and toughness. The elastomer exhibits remarkable tensile strength (~82.5 ± 3.9 MPa) and toughness (~470 ± 29 MJ/m^3), notably strain-stiffening behavior, and ultra-high fracture resistance (384.7 ± 18.9 kJ m^{-2}). Polycaprolactone (PCL) segment is used to endow biodegradability and shape memory. With appropriate microphase separation, the PCL segments can crystallize at low temperatures with the end temperature of melting around 37°C, realizing shape memory at body temperature. The obtained elastomer is 4D printable and verified to be biocompatible at the cellular, blood, and animal levels. Transcriptome results indicate that the elastomer up-regulates genes related to cell proliferation and has great potential in the field of tissue repair.

[1]Advanced Materials Laboratory of Ministry of Education (MOE), Department of Chemical Engineering, Tsinghua University, Beijing 100084, China. [2]State Key Laboratory for Quality Ensurance and Sustainable Use of Dao-di Herbs, Artemisinin Research Center, and Institute of Chinese Materia Medica, China Academy of Chinese Medical Sciences, Beijing 100700, China.
*Corresponding author. Email: cqiu@icmm.ac.cn (C.Q.); jun-xu@mail.tsinghua.edu.cn (J.X.)

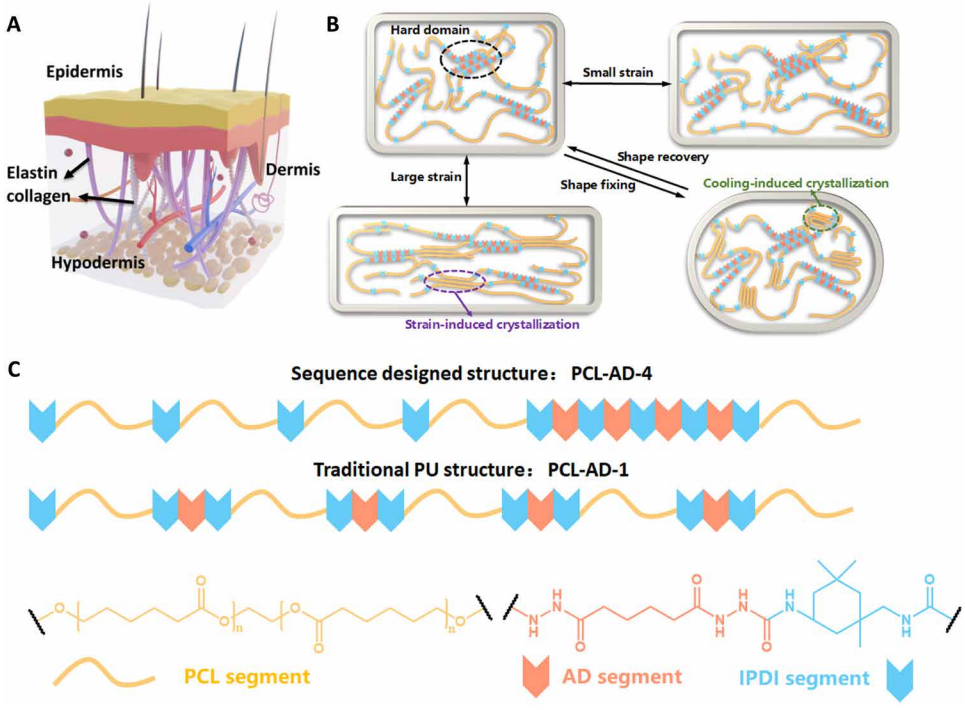

Fig. 1. Design and structure of skin-like elastomer PCL-AD-4. (**A**) Interwoven structure of elastin and collagen in skin tissue. (**B**) Schematic diagram of the structural evolution of PCL-AD-4 in small deformation, large deformation, and shape memory cycles. (**C**) Chemical structure of PCL-AD-4 and PCL-AD-1.

RESULTS

Elastomer synthesis

The target elastomer is prepared by a one-pot prepolymerization-chain extension (two step) method (fig. S1). PCL diol with number-average molecular weight (M_n) = 2000 is selected as the soft segment, isophorone diisocyanate (IPDI) and adipic dihydrazide (AD) are used as the linking agent and chain extender to form the hard segment. To control the sequence length of the segments, PCL diol first reacts with IPDI in different proportions for prepolymerization to obtain prepolymers with an average of one to four PCL segments with two terminal isocyanates. Then, the remaining IPDI and AD are added to ensure a total molar ratio of PCL:IPDI:AD = 1:2:1. The obtained four PUs are named as PCL-AD-X, where X can be 1, 2, 3 and 4, representing the average number of PCL segments in the prepolymer. H^1–nuclear magnetic resonance (NMR) spectra and molecular weights of the synthesized materials are listed in the Supplementary Materials. Among them, PCL-AD-1 and PCL-AD-4 show the most notable difference, and the following discussion will mainly focus on the two samples.

In PCL-AD, PCL soft segments provide crystallinity and degradability, while IPDI-AD hard segments form hydrogen bond arrays to provide mechanical strength. Just as in the above skin-inspired molecular design strategy, low hard segment content [23.63 weight % (wt %)] and the strong aggregation tendency of hydrogen bond arrays ensure a low modulus. A longer block sequence (such as PCL-AD-4) not only enhances the stability of the hard domain by promoting microphase separation but also improves the crystallization ability of PCL to achieve an improvement in strain-stiffening through strain-induced crystallization (Fig. 1, B and C).

Figure 1B shows the mechanism of realizing body-temperature shape memory with long sequences. According to Flory-Huggins theory, longer segment sequences are more conducive to generate microphase separation (*26*). For example, in PCL-AD-1, the microphase separation is weak since most of the hard segments are mixed with the PCL soft segment, which limits PCL crystallization. In PCL-AD-4, the long sequence of soft and hard segments results in strong microphase separation, making the hard segments aggregate into nanometer-sized hard domains, which act as strong physical crosslinking points. On the other hand, the long sequence of PCL soft segments leads to strong tendency of crystallization. The hard domains not only serve as the fixed phase to improve the shape recovery rate during the shape memory process but also limit the excessive crystallization of PCL, reduce the lamellar size, and depress the melting temperature below 37°C. Therefore, the arrangement of soft/hard segments is the key to achieve body-temperature shape memory.

Mechanical performance and mechanism

The typical stress-strain curves of the samples are shown in Fig. 2A. Compared with PCL-AD-1, PCL-AD-4 has a similar initial modulus (~3.0 MPa versus ~3.7 MPa), but a significant increase of tensile strength (~82.5 MPa versus ~50.2 MPa), exhibiting a clear J-shaped stress-strain curve with a relatively low initial modulus and intense strain-stiffening characteristics. The soft-while-strong PCL-AD-4 still maintained a high elongation at break of ~1627%, leading to a toughness of ~470 MJ/m^3, which was a 1.6-fold increase as compared to PCL-AD-1. Considering the markedly decreased cross-sectional area of elastomers at break, the true stress-strain curve was used to more accurately describe the mechanical behaviors of the highly extensible elastomers. This high strength and elongation of PCL-AD-4 correspond to a true stress at break as high as 1.42 GPa, which is greater than that of spider silks (fig. S9) (*27*–*29*).

The normalized elastic modulus defined as $E_0^{-1}d\sigma_{true}/d\lambda$ is adopted to evaluate the strain-stiffening characteristic, where λ is the

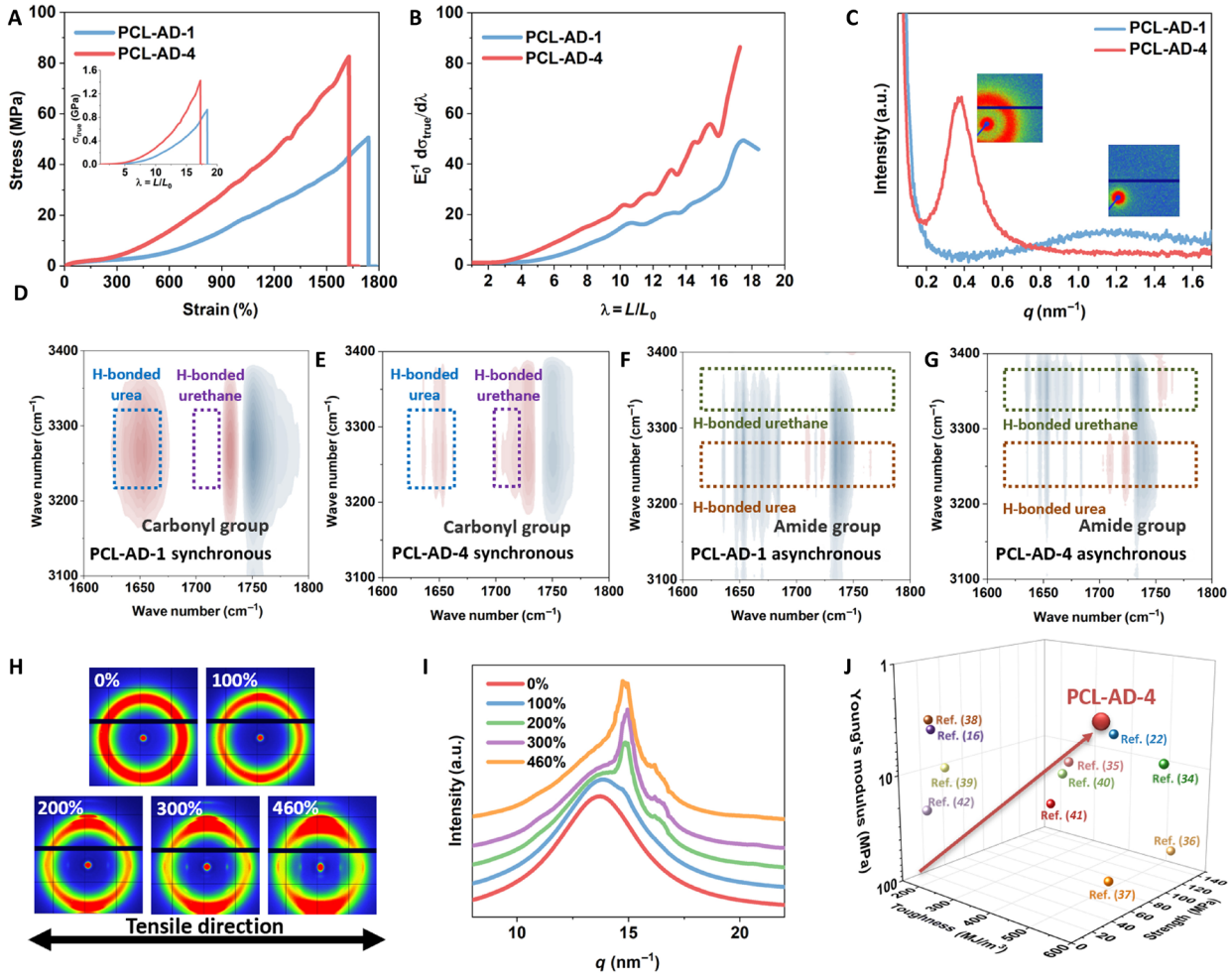

Fig. 2. Tensile properties, microphase separation, and hydrogen bonds. (**A**) Engineering and true stress-strain curves of PCL-AD-1 and PCL-AD-4. (**B**) Normalized modulus-strain curves of PCL-AD-1 and PCL-AD-4. (**C**) 1D SAXS curves and 2D SAXS images of the samples. (**D** and **E**) Synchronous and (**F** and **G**) asynchronous 2D correlation FTIR spectra of PCL-AD-1 and PCL-AD-4. (**H**) In situ stretched WAXD 2D images of PCL-AD-4. (**I**) In situ tensile WAXD 1D curves of PCL-AD-4. (**J**) Comprehensive comparison of the Young's modulus, strength, and toughness of PCL-AD-4 with other high-performance elastomers (*16*, *22*, *34*–*42*).

deformation ratio, σ_{true} is the true stress, and E_0 is the initial modulus. PCL-AD-4 exhibits a J-shaped curve in Fig. 2B, demonstrating a remarkable 86-fold increase in the differential modulus within the elongation at break, which is similar to that of biological tissues (*9*). PCL-AD-4 exhibits a two-stage process during tensile deformation. When λ is lower than 3, the mechanical behavior of PCL-AD-4 is almost identical to that of PCL-AD-1. However, at a larger λ, the structural differences caused by the long sequence led to stronger strain-stiffening in PCL-AD-4.

The mechanical behavior of PCL-AD-4 originates from multiple aspects. Small-angle x-ray scattering (SAXS) results prove that segment arrangement can significantly affect the microphase separation structure (Fig. 2C). PCL-AD-1 has only a weak scattering peak with the long period size of approximately 5.7 nm, while PCL-AD-4 exhibits a strong scattering peak with the long period size of approximately 16.1 nm. Strengthened microphase separation can greatly improve the mechanical properties of elastomers, mainly due to the enhanced physical crosslinking. The Fourier transform infrared (FTIR) spectroscopy analysis of the carbonyl region shows the content of hydrogen bonds in PCL-AD-4 is not significantly increased compared to PCL-AD-1 (fig. S11 and table S4), but the sequential breakage and reorganization of the hierarchical weak to strong hydrogen bonds under external disturbances of the two samples is quite different. As a dynamic interaction, hydrogen bonds can dissipate stress concentration through dissociation-recombination during stretching, improving strength and toughness. Figure 2 (D to G) shows the carbonyl-amino interaction in PCL-AD-1 and PCL-AD-4. In the synchronous spectrum, PCL-AD-4 shows correlation peaks related to hydrogen-bonded urethane and urea carbonyl, while PCL-AD-1 only has correlation peaks related to hydrogen-bonded urea carbonyl. The asynchronous spectrum shows that the change of hydrogen-bonded amino groups in PCL-AD-4 mainly arises from the urethane amino, while that in PCL-AD-1 is from the urea amino. In summary, PCL-AD-4 exhibits multilevel hydrogen bonding response, with weak hydrogen bonds preferentially breaking during stretching while strong hydrogen bonds maintaining the stability of intermolecular physical cross-linking. On the contrary, PCL-AD-1 lacks multilevel hydrogen bonding response, and most of the hydrogen bonds are broken during stretching, leading to molecular chain slip and material failure. Figure 2 (H and I) presents the wide-angle

x-ray scattering (WAXS) results of PCL-AD-4 during the stretching, proving the existence of strain-induced crystallization. As the strain increases, two peaks located at q = 14.7 and 16.8 nm^{-1} appear, corresponding to the (110) and (200) crystal planes of PCL, respectively. Strain-induced crystallization can form new physical crosslinks under large deformations and promote strain hardening (*30*–*32*). It should be noted that before stretching, PCL-AD-4 has no crystallization signal, meaning that it is in an amorphous elastomeric state at room temperature. Different from those elastomers strengthened based on initial microcrystals (*33*), the mechanical behavior of PCL-AD-4 come from structural evolution during the tensile process, such as dissociation/recombination of hydrogen bonds and strain-induced crystallization.

The reported elastomers with extremely high strength and toughness usually cannot achieve a low modulus. Therefore, comprehensively considering the three indicators of initial modulus, strength, and toughness, PCL-AD-4 has an advantage over the previously reported high-performance elastomers (Fig. 2J) (*16*, *22*, *34*–*42*).

The puncture resistance of PCL-AD-4 is prominent. A film with a thickness of only 0.15 mm can withstand puncture stroke of a tip as high as 35.5 mm (Fig. 3A), meaning that it can prevent damage from sharp objects such as needles in medical applications. Because of the presence of hydrogen bond arrays and strain-induced crystallization in PCL-AD-4, the crack tolerance is also excellent. The crack tolerance is determined by the Green-Smith method (*17*, *43*, *44*). A 1-mm-wide notch is prefabricated on a rectangular sample of 5 mm by 10 mm by 1 mm, and the sample can still be stretched to a strain as high as 1200% and a stress of 47 MPa before fracture occurs (Fig. 3B). During the loading process, the crack does not expand rapidly but blunted (fig. S13), which can be attributed to hydrogen bonds dissipating the stress concentration at the tip and strain-induced crystallization hindering crack propagation at the same time (*45*). The fracture energy of PCL-AD-4 is calculated to be 384.7 ± 18.9 kJ/m^2, which exceeds that of skin (3.6 kJ/m^2) by ≈107-fold and surpasses the highest tear energy (103.7 kJ m^{-2}) reported for skin-like materials (*42*). Up to our knowledge, even compared to all the reported high-strength and tough elastomers, the fracture energy of PCL-AD-4 is still in the first echelon (Fig. 3C) (*22*, *34*, *40*, *46*–*50*).

In practical applications, skin-like elastomers usually face various complex working conditions, especially different strain rates. Under the different tested strain rates, the tensile curves of PCL-AD-4 almost coincide, meaning that the flexibility does not change significantly (fig. S14). The cyclic tensile curves of PCL-AD-4 under gradually increasing strains (fig. S15) reflect a significant Mullins' effect (*51*, *52*). This means that damage to the physical cross-linking network will occur during strain, but the degree of damage depends on the maximum strain. In the actual working conditions of elastomers, such as artificial heart valves, eardrums, and patches, repeated small deformations are very common. Therefore, a dynamic mechanical analysis (DMA) instrument was used to test the material at 10% deformation for 100,000 cycles at 37°C (Fig. 3D). The results show that except for a small proportion of stress attenuation in the initial stage due to the adaptive reorganization of hydrogen bonds, the stress remains stable in the later stage. This means that PCL-AD-4 has satisfying fatigue resistance. Stress relaxation (Fig. 3E) results show that the relaxation activation energy (E_a) of PCL-AD-4 reaches as high as 104 kJ/mol, which is at the same level as many dynamically covalent networks (*53*). Such a high E_a is attributed to the strong microphase separation formed by long hydrogen bond arrays in the hard domains (*49*, *54*).

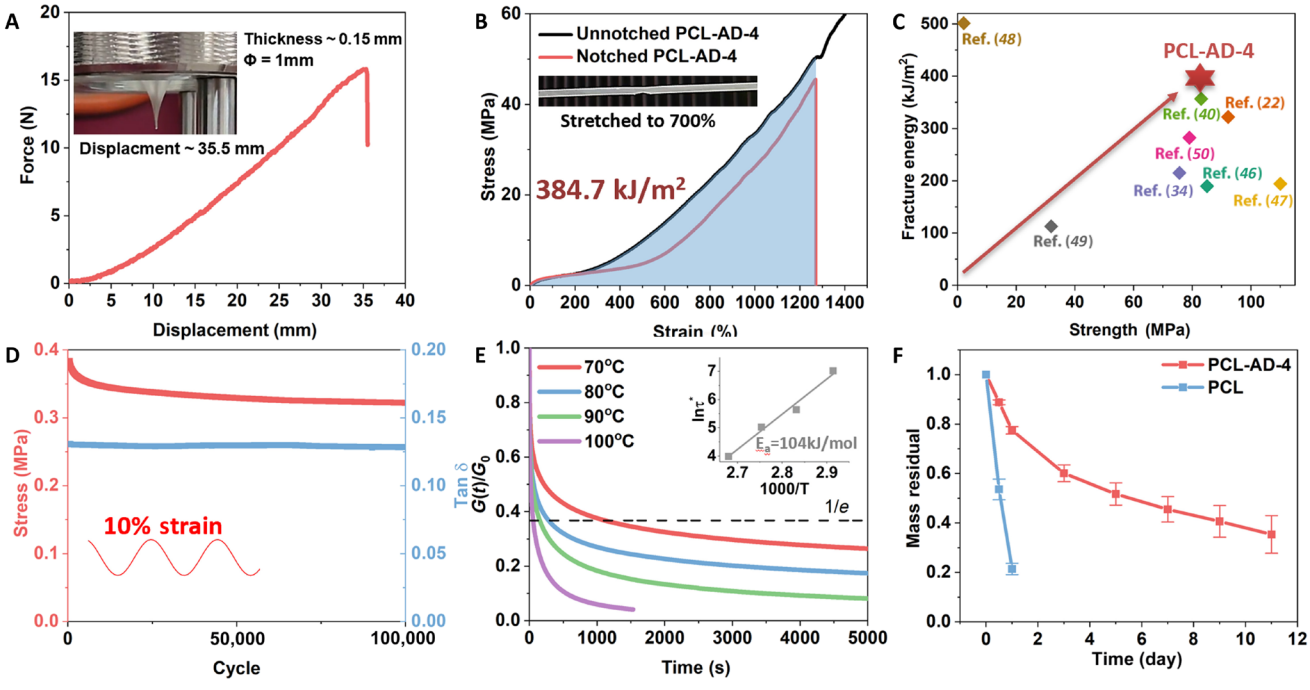

Fig. 3. The damage tolerance and biodegradable of PCL-AD-4. (**A**) Photograph and force-displacement curve of the PCL-AD-4 film in the puncture test. (**B**) Tensile test of single-notched PCL-AD-4 specimen. (**C**) Comparison of the strength and fracture energy of PCL-AD-4 with those of elastomers reported in the literature (*22*, *34*, *40*, *46*–*50*). (**D**) Stress and tanδ variation of PCL-AD-4 during 100,000 cycles of 10% sinusoidal oscillation testing. (**E**) Stress relaxation curves and relaxation time-temperature Arrhenius fit of PCL-AD-4. (**F**) Mass loss curve of PCL and PCL-AD-4 in the presence of keratinase.

As we all know, PCL can degrade under natural and biological conditions and has extensive applications in the medical field. Here, we use keratinase to degrade PCL and PCL-AD-4 in phosphate-buffered saline buffer. As shown in Fig. 3F, because of the presence of hard segments and physical cross-linking, the degradation rate of PCL-AD-4 is lower than that of pure PCL, but it can still achieve sufficient degradation. Generally, pure PCL takes over half a year to degrade in the human body. Therefore, we expect that PCL-AD-4 can achieve a service life that spans several years in the human body. This characteristic of slow degradation is particularly suitable for implant materials that need to maintain performance for a long time in vivo. It is worth mentioning that although the PCL segments in PCL-AD-4 were degraded, the mechanical properties could still be maintained at a relatively high level. For example, after 11 days of keratinase degradation, its mass residue was less than 40%, while the tensile strength could still exceed 10 MPa (fig. S16).

Body-temperature shape memory and 4D printing

After confirming that PCL-AD-4 has excellent mechanical behaviors, its body-temperature shape memory performance was evaluated. First, as indicated by the DMA curves (Fig. 4A and fig. S17), PCL-AD-1, PCL-AD-2, and PCL-AD-3 all exhibit typical thermomechanical behavior of amorphous thermoplastic elastomers. Although PCL-AD-4 is amorphous at room temperature, after cooled in the DMA furnace, the storage modulus slowly rises below 0°C, corresponding to the crystallization of PCL. More encouragingly, the starting temperature of the elastic plateau modulus of PCL-AD-4 is exactly around 37°C, corresponding to the complete melting of PCL crystals. This temperature responsiveness meets the requirement of body-temperature shape memory. Further differential scanning calorimetry (DSC) and x-ray diffraction (XRD) analysis reveal that PCL-AD-4 can completely crystallize in an hour at −20°C and completely melt at 37°C (Fig. 4B and fig. S18). This crystallization behavior originates from strong microphase separation and a moderate crystallization ability of long sequences of PCL segments.

Extrapolating from the Arrhenius equation, the relaxation time of PCL-AD-4 at body temperature reaches up to 47,500 s, indicating that the physical cross-linking is stable. Meanwhile, the crystallization-melting characteristics have also been clarified. Thus, the shape memory performance of PCL-AD-4 is expected to be excellent. Fig. 4C shows the temperature-stress-strain correlation curves of two consecutive shape memory cycles. PCL-AD-4 has an extremely high shape fixation rate (~100%), and the shape recovery rate exceeds 94% (see Supplementary Materials for details). Figure 4D demonstrates the shape recovery process of PCL-AD-4 after being shaped by freezing crystallization and placed on human palm. The U-shaped and twisted splines can almost recover to the original straight shape within 30 s on the palm.

We used the designed materials to simulate a simple minimally invasive surgery (MIS) process (fig. S20). PCL-AD-4 with a permanent spring-like shape was shaped into a straight line by freezing crystallization and loaded into an injection catheter and then slowly injected into water at body temperature. The material quickly recovered to the spring shape after injection. In practical medical applications, the fabrication and customization of materials with complex structures are highly essential. For this purpose, we further investigated the 4D printability of PCL-AD-4. Figure 4E shows that the gel-sol transition temperature of PCL-AD-4 is ~180°C. When the temperature exceeds 180°C, the melt viscosity continuously decreases (Fig. 4F). Thus, PCL-AD-4 is capable of 4D printing under appropriate conditions. Figure 4 (G to I) presents three typical applications, such as vascular stents (*55*), myocardial patches (*56*), and intervertebral disc scaffolds (*57*) with negative Poisson's ratio. Each 4D printed sample can achieve compression and expansion through the shape memory process, and the excellent shape recovery ratio ensures that the complex structures do not undergo deformation or failure. The 4D printability of PCL-AD-4 reveals its broader application prospects.

Biosafety evaluation

As a material targeted for biomedical applications, it is necessary to conduct biosafety assessments of PCL-AD-4. In all the experiments, medical PCL was selected as a control material to investigate the biosafety of PCL-AD-4 in vitro and in vivo, including the cell proliferation and viability assay, erythrocyte agglutination and hemolysis assay, subcutaneous transplantation experiment in vivo, and so on.

Firstly, to investigate the effect on the proliferation of normal cells, human immortalized keratinocyte cell (Hacat) and human umbilical vein endothelial cell (Huvec) were selected as the model cells. PCL-AD-4 and PCL materials were cut into thin slices and cocultured with Hacat and Huvec cells. As shown in Fig. 5A, Hacat and Huvec cells could adhere and grow on the surface of PCL-AD-4 [from (1) to (2)]. Compared with PCL, the slow degradation of PCL-AD-4 also did not affect the adherent proliferation of cells [from (2) to (3)] with a same growth rate without significant difference as the control [(3)]. The apoptosis rates (early apoptosis and late apoptosis rates of <5%) of PCL-AD-4 groups on Hacat and Huvec cells were similar to those of the blank, demonstrating the nontoxic cell ability of PCL-AD-4 (Fig. 5B and fig. S21). However, PCL-AD-4 had the lower apoptosis rates than PCL, indicating better biosafety.

If the material causes red blood cell agglutination, then it would lead to blood vessel blockage (*58*). To confirm the potential use as a vascular implant material, the agglutination and hemolysis assay of red blood cells were used to detect the blood compatibility of PCL-AD-4. As shown in Fig. 5C and fig. S20, PCL-AD-4 neither induced hemagglutination such as PEI_{25k} material nor hemolysis like Triton X-100, indicating the same hemocytic safety as PCL and blank group. Moreover, the components in the body's circulation are more complex, and the interference of serum protein and growth factor poses a threat to the safety and stability of PCL-AD-4. Therefore, serum was used as a simulated environment to examine the stability of the materials by detecting the dissolution state of the materials in the serum. The results of serum stability indicated that PCL-AD-4 exhibited no significant serum instability within 24 hours with PCL and blank group (Fig. 5D). These results suggested that PCL-AD-4 had a high level of safety for both in vitro and in vivo potential application.

To avoid side effects of PCL-AD-4 in vivo, such as causing inflammation or inhibiting wound healing, we investigated the in vivo safety of PCL-AD-4 by inoculating the material into skin on the backs of mice (Fig. 6A). The wound healing of mice in all groups was satisfactory after 14 days of recovery with no significant difference. However, it was found that PCL-AD-4 slices did not dissolve or degrade significantly in 14 days, proving its characteristic of slow degradation. The hematoxylin and eosin staining of skin shown that skin cells could grow around the PCL-AD-4 slices, indicating that implantation do not affect wound healing. After hematoxylin and eosin staining of mouse organs (Fig. 6B), it could be seen that PCL-AD-4 did not cause organic changes in organs compared with PCL and the control groups. Meanwhile, the blood routine and biochemical

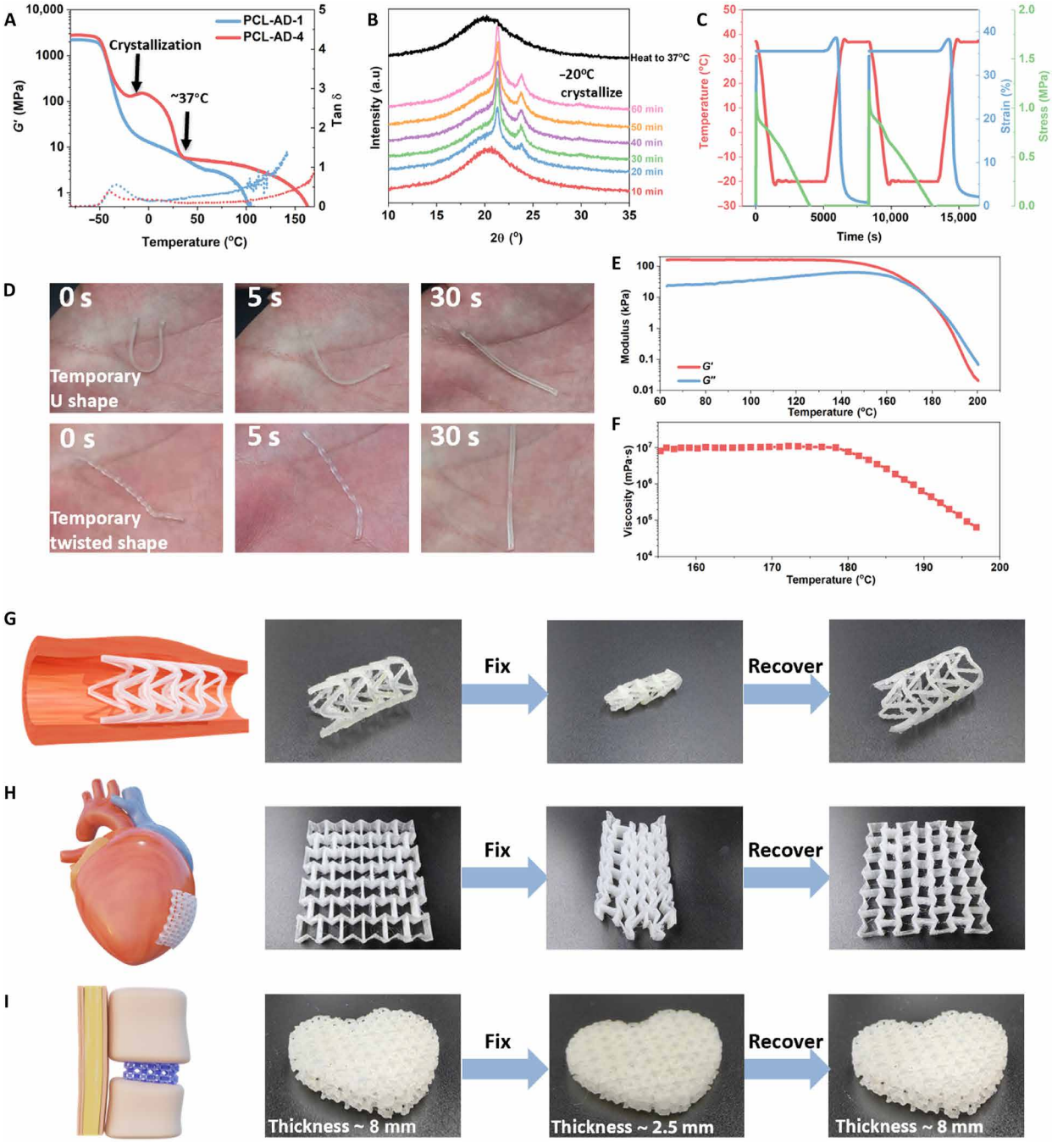

Fig. 4. Body-temperature shape memory and 4D printing of PCL-AD-4. (**A**) DMA curves of the samples. (**B**) XRD curves of PCL-AD-4 at different temperatures and times. (**C**) Shape memory curves of PCL-AD-4. (**D**) Process of body-temperature shape memory on the palm. (**E**) Dynamic rheological curve of PCL-AD-4 at a frequency of 1 Hz. (**F**) Viscosity-temperature curve of PCL-AD-4 at a shear rate of 1 s^{-1}. 4D printed PCL-AD-4 components: (**G**) vascular stent, (**H**) myocardial patch with negative Poisson's ratio, and (**I**) intervertebral disc scaffolds with negative Poisson's ratio.

indexes of the mice were detected on the 7th and 14th day. All indices of mice in the experimental group and control group were within the normal range (Fig. 6, C and D). The changes in body weight of the mice (Fig. 6E) also reflected the in vivo safety of PCL-AD-4. Above all, these results proved that the PCL-AD-4 had a good safety in in vivo application.

To further investigate the potential biological functions, we examined the effect of PCL-AD-4 on gene expression of HUVEC cells using bulk RNA sequencing analysis. The differential expression genes (DEGs) number between PCL-AD-4 and PCL was low ($n = 42$) (Fig. 7A), indicating that there was not a significant difference in the impact of PCL-AD-4 and PCL on gene expression. It is known that PCL promotes the proliferation of HUVECs and can induce endothelialization when used as a vascular implant material (*59*, *60*). Therefore, we want to know whether PCL-AD-4 has similar functions. To identify the changed gene expression pattern and enriched pathways,

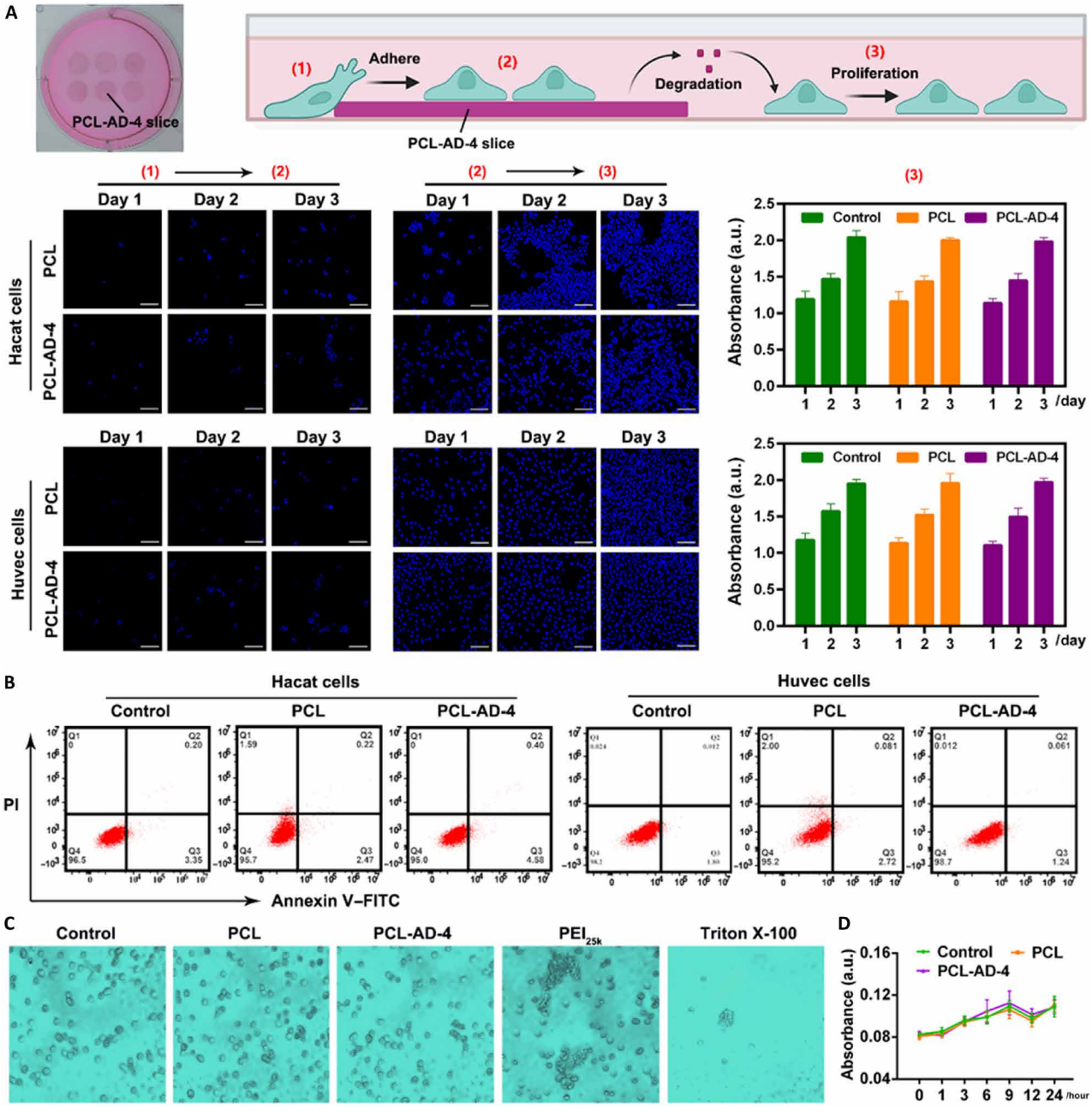

Fig. 5. Cell and blood compatibility. (**A**) Cell viability affection of PCL and PCL-AD-4 on Hacat and Huvec cells. (Scale bar: 25 μm). n = 3, mean ± SD. (**B**) The apoptosis effect of PCL and PCL-AD-4 on Hacat and Huvec cells. (**C**) Erythrocyte agglutination assay with PCL and PCL-AD-4. (**D**) Serum stabilization of PCL and PCL-AD-4. *n* = 6, means ± SD.

we investigated the differentially DEGs analysis between PCL-AD-4 and control group, which revealed a total of 1218 (1194 up, 24 down) DEGs (|fold change| ≥ 2, $P < 0.05$) (Fig. 7B). Gene Ontology (GO) enrichment of these up-regulated genes in PCL-AD-4 group evidenced the activated pathways that were associated with cell proliferation, such as DNA replication, cell cycle checkpoint signaling, and regulation of cell morphogenesis (Fig. 7C). Furthermore, the gene set enrichment analysis (GSEA) based on DEGs of PCL-AD-4 group versus control group indicated that the cell cycle signaling pathway in PCL-AD-4 group was increased (*P* value = 0.000167) (Fig. 7D). Also, the expression of cell cycle regulated gene sets was up-regulated in the PCL-AD-4 group compared with the control group (Fig. 7E). These findings implied that PCL-AD-4 could promote Huvec cells proliferation and development, suggesting its potential ability in vascular implantation and other disease treatments. Meanwhile, these changes were also observed in the effects of PCL-AD-4 in Hacat cells. Meaningfully, it was found that regulation of response to DNA damage stimulus and regulation of DNA repair were up-regulated in PCL-AD-4 group compared with PCL group (fig. S23), indicating that PCL-AD-4 might have a better bioactivity in cell or tissue repair treatment.

In summary, PCL-AD-4 exhibits functions that promote proliferation, development, and repair in different cells. Although the specific

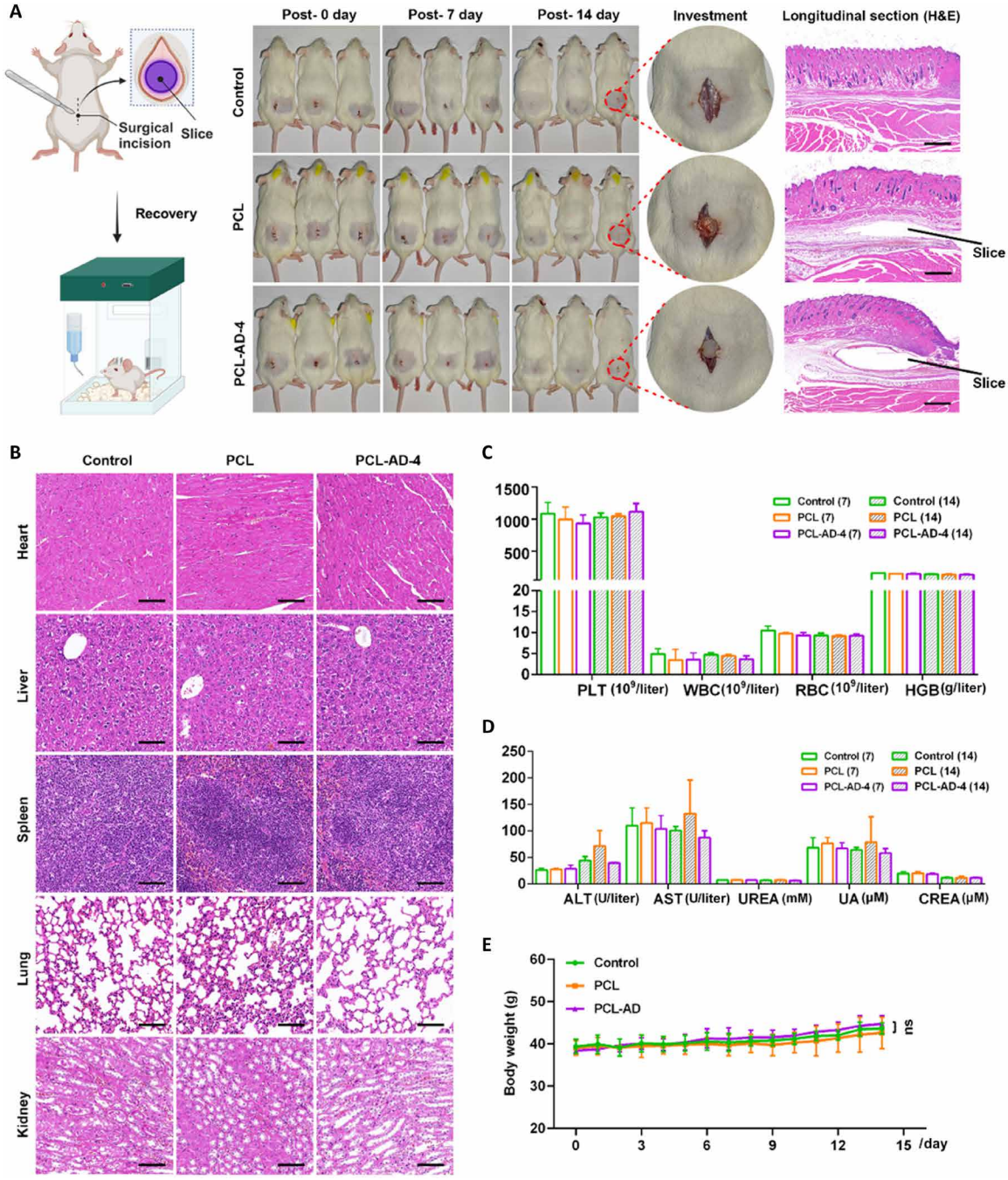

Fig. 6. The in vivo safety. (**A**) Effect of PCL or PCL-AD-4 slice implantation on wound healing. (**B**) Hematoxylin and eosin (H&E) staining of heart, liver, spleen, lung, and kidney of mice after 14 days of embedding. Scale bar, 200 μm. (**C**) Routine blood changes [platelet (PLT), white blood cell (WBC), red blood cell (RBC), and hemoglobin (HGB)] in mice after 7 days and 14 days of wound healing. (**D**) Changes in biochemical factors [aminotransferase (ALT), aspartate aminotransferase (AST), UREA, uric acid (UA), and creatinine (CREA)] in mice after 7 and 14 days of wound healing. (**E**) Body weight changes in mice within 14 days after embedding the material. $n = 3$, means ± SD.

mechanism needs further exploration, it strongly demonstrates the good potential of PCL-AD-4 in the biomedical engineering field.

DISCUSSION

An elastomer PCL-AD-4 that combines damage resistance, body temperature shape memory, biodegradability, and biosafety was obtained via block design. To the best of our knowledge, PCL-AD-4 represents a pioneering example in emulating both mechanical and structural properties of skins, encompassing nonlinear mechanical behavior, exceptional strength, and damage tolerance. The skin-like mechanical properties were readily achieved by rational combination of hydrogen bonds, microphase separation, and crystallization. As a result, PCL-AD-4 exhibits an exceptional true stress at break of 1.42 GPa,

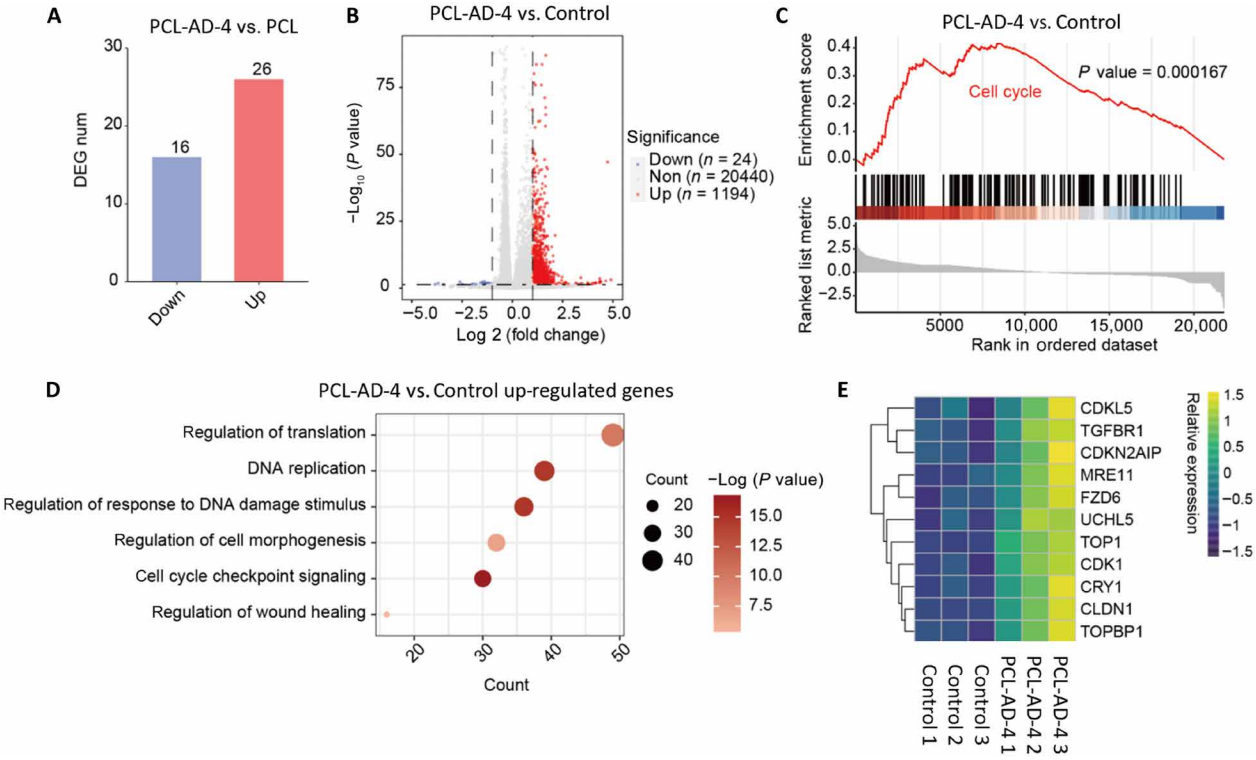

Fig. 7. Bulk RNA sequencing analysis. (**A**) Bar plots depicting the differentially expressed genes (DEGs) number of down-regulated genes and up-regulated genes between PCL-AD-4 versus PCL in Huvec cells. (**B**) Volcano plots show the DEGs between PCL-AD-4 versus control in Huvec cells. The *x* axis illustrates the log 2 fold change (FC), and the *y* axis indicates as –log (*P* value). The color of scatter point indicates the changed type of differentially expressed genes or proteins (red, up; gray, not significance; blue, down). (**C**) GSEA plot demonstrates that PCL-AD-4 group up-regulated cell cycle signaling pathway compared with control group in Huvec cells. (**D**) Bubble plot shows the GO enrichment biological process items of PCL-AD-4 group versus control group up-regulated DEGs in Huvec cells. (**E**) Heatmap shows the gene relative expression level of samples of PCL-AD-4 and control groups in Huvec cells. ns, not significant.

and super damage tolerance with a high fracture energy of 384.7 kJ/m^2 and high puncture force. The regulation of crystallization of soft blocks endows PCL-AD-4 with excellent body-temperature shape memory properties and supports 4D printing for customizing the required biomedical products. The biosafety of PCL-AD-4 has been demonstrated through three aspects of evaluations: cells, blood, and subcutaneous implantation in mice. Transcriptome experiments reveal that PCL-AD-4 has an unexpected function of promoting cell proliferation and DNA repair. These excellent properties and potential biological functions make PCL-AD-4 have great application potential in the biomedical engineering field.

Elastomers have been widely used throughout society, ranging from household goods and car tires to tissue engineering. Although there have been advancements in the synthesis and applications of elastomers in modern age, the molecular design strategies that meet the requirements of complex properties have remained almost unchanged. Here, we report the next-generation biomedical elastomers with body-temperature shape memory that can achieve skin-like properties through a multiscale mechanism, which are far superior to other common materials. Because of the complex coupling of its structure-property relationships, PCL-AD-4 also requires further fundamental research. Generally, the modular block design approach adopted here provides a promising platform in the field of elastomers. Through the comprehensive design of the chemical and sequence structures of blocks, the elastomers fabricated in this manner exhibit the capacity to outperform conventional counterparts. This class of new elastomers can play a key role in the future of aerospace structures, medical devices, and soft robots.

MATERIALS AND METHODS

Materials

Polycaprolactone diol [PCL 220N, Daicel (China) Investment Co., Ltd., M_n = 2000 g mol^{-1}] was dried under vacuum at 110°C before use. IPDI (99%), AD (98%), dibutyltindilaurate (DBTDL; 98%), and dimethylacetamide (DMAc; ultra dry, 99%) were purchased from Admas-Beta. All reagents were used as received except PCL.

Prepolymerization of PCL and IPDI

Four types of prepolymers were prepared using a one-pot process, and the feeding ratios for each sample are presented in table S1. In a representative procedure, 10.00 g (5 mmol) of PCL 220N, 2.22 g (10 mmol) of IPDI, 0.01 g of DBTDL (0.1 wt % of PCL), and 5 ml of DMAc were mixed. The mixture was then heated to 80°C and stirred for 3 hours. The gel permeation chromatography (GPC) results for the prepolymer can be found in table S1.

Preparation of PCL-AD by chain extension of prepolymers

After synthesizing the prepolymer, a solution of IPDI and AD in 60 ml of DMAc was added to the prepolymer at 40°C and stirred for 24 hours. The resulting mixture was then degassed under vacuum to remove any bubbles. Subsequently, the mixture was poured onto a Teflon

plate and preliminary volatile solvent for 12 hours at 80°C. To obtain a polymer sheet, the polymer was further dried under vacuum at 60°C for ~72 hours. The feeding ratios and GPC results for different samples can be found in table S2.

General characterization

FTIR spectra were collected on a Nicolet 6700 FTIR spectrophotometer equipped with a deuterated triglycine sulfate detector. Each sample was cast onto a KBr plate to obtain a thin film. The transmission spectra were collected with an average of 16 scans for each run at a resolution of 4 cm^{-1} in the range of 4000 to 500 cm^{-1}. GPC test was carried out on Agilent 1260 with Plgel 5-μm MIXED-C column under tetrahydrofuran mobile phase. DSC measurement was conducted on a DSC 250 (TA Instrument) under nitrogen atmosphere. DMA was carried out on a DMA Q850 apparatus (TA Instrument) in a tension film mode with a heating rate of 3°C min^{-1}. The maximum strain was 0.05%, and the frequency was 1 Hz. The stress relaxation test was also carried out on a DMA Q850 in a tension film mode. After a 5-min equilibration at the preset temperature, the samples underwent a tensile relaxation test with a strain of 5%. Dumbbell-shaped specimens for tensile tests were cut from cast sheets using a standard bench-top die according to GB/T-528 [~1 mm(thickness) × 2 mm(width) × 35 mm(length) and a gauge length of 10 mm]. Tensile tests were conducted on a JinJian UTM-1432 tensile tester equipped with a 500 N load cell. SAXS measurement was conducted on a Xenocs Xeuss 1.0. In situ WAXS test was carried on Xenocs Xeuss 3.0. Rheological testing was conducted on Anton Paar MCR301 in parallel plate mode.

4D printing of PCL-AD-4

PCL-AD-4 was made into a wire with a diameter of ~1.75 mm and printed using Bambu X1 at a nozzle temperature of 230°C. The volume filling rate is 100%, and the layer height is 0.1 mm. Other materials and methods are shown in the Supplementary Materials.

Supplementary Materials

This PDF file includes:

Supplementary Methods
Tables S1 to S6
Figs. S1 to S23

REFERENCES AND NOTES

1. H. Kim, H. Jang, B. Kim, M. K. Kim, D. S. Wie, H. S. Lee, D. R. Kim, C. H. Lee, Flexible elastomer patch with vertical silicon nanoneedles for intracellular and intratissue nanoinjection of biomolecules. *Sci. Adv.* **4**, eaau6972 (2018).
2. C. Cui, L. Mei, D. Wang, P. Jia, Q. Zhou, W. Liu, A self-stabilized and water-responsive deliverable coenzyme-based polymer binary elastomer adhesive patch for treating oral ulcer. *Nat. Commun.* **14**, 7707 (2023).
3. L. Wu, A. Magaz, S. Huo, A. Darbyshire, M. Loizidou, M. Emberton, M. Birchall, W. Song, Human airway-like multilayered tissue on 3D-TIPS printed thermoresponsive elastomer/collagen hybrid scaffolds. *Acta Biomater.* **113**, 177–195 (2020).
4. U. Sharma, D. Concagh, L. Core, Y. Kuang, C. You, Q. Pham, G. Zugates, R. Busold, S. Webber, J. Merlo, R. Langer, G. M. Whitesides, M. Palasis, The development of bioresorbable composite polymeric implants with high mechanical strength. *Nat. Mater.* **17**, 96–103 (2018).
5. H. C. Wang, S. Cui, F. Niu, Optimization and demonstration of two types of spring-roll dielectric elastomer actuators for minimally invasive surgery. *Front. Bioeng. Biotechnol.* **10**, 1016350 (2022).
6. E. Dashtimoghadam, F. Fahimipour, A. N. Keith, F. Vashahi, P. Popryadukhin, M. Vatankhah-Varnosfaderani, S. S. Sheiko, Injectable non-leaching tissue-mimetic bottlebrush elastomers as an advanced platform for reconstructive surgery. *Nat. Commun.* **12**, 3961 (2021).
7. R. Akman, H. Ramaraju, S. J. Hollister, Development of photocrosslinked poly(glycerol dodecanedioate)—A biodegradable shape memory polymer for 3D-printed tissue engineering applications. *Adv. Eng. Mater.* **23**, 2100219 (2021).
8. J. Wang, B. Wu, P. Wei, S. Sun, P. Wu, Fatigue-free artificial ionic skin toughened by self-healable elastic nanomesh. *Nat. Commun.* **13**, 4411 (2022).
9. M. Vatankhah-Varnosfaderani, A. N. Keith, Y. Cong, H. Liang, M. Rosenthal, M. Sztucki, C. Clair, S. Magonov, D. A. Ivanov, A. V. Dobrynin, S. S. Sheiko, Chameleon-like elastomers with molecularly encoded strain-adaptive stiffening and coloration. *Science* **359**, 1509–1513 (2018).
10. W. Zhang, B. Wu, S. Sun, P. Wu, Skin-like mechanoresponsive self-healing ionic elastomer from supramolecular zwitterionic network. *Nat. Commun.* **12**, 4082 (2021).
11. S. Chen, L. Sun, X. Zhou, Y. Guo, J. Song, S. Qian, Z. Liu, Q. Guan, E. Meade Jeffries, W. Liu, Y. Wang, C. He, Z. You, Mechanically and biologically skin-like elastomers for bio-integrated electronics. *Nat. Commun.* **11**, 1107 (2020).
12. Y. Chen, P. G. Miller, X. Ding, C. E. T. Stowell, K. M. Kelly, Y. Wang, Chelation crosslinking of biodegradable elastomers. *Adv. Mater.* **32**, 2003761 (2020).
13. X. Yang, Z. Han, C. Jia, T. Wang, X. Wang, F. Hu, H. Zhang, J. Zhao, X. Zhang, Preparation and characterization of body-temperature-responsive thermoset shape memory polyurethane for medical applications. *Polymers* **15**, 3193 (2023).
14. H. Guo, R. Puttreddy, T. Salminen, A. Lends, K. Jaudzems, H. Zeng, A. Priimagi, Halogen-bonded shape memory polymers. *Nat. Commun.* **13**, 7436 (2022).
15. J. Qin, Y. Chen, X. Guo, Y. Huang, G. Chen, Q. Zhang, G. He, S. Zhu, X. Ruan, H. Zhu, Regulation of hard segment cluster structures for high-performance poly(urethane-urea) elastomers. *Adv. Sci.* **11**, 2400255 (2024).
16. H. Chen, Z. Sun, K. Lu, J. Liu, C. He, D. Mao, Negative enthalpy variation drives rapid recovery in thermoplastic elastomer. *Adv. Mater.* **35**, 2311332 (2023).
17. T. Liu, C. L. Li, H. Yao, F. Y. Sun, L. Wang, B. W. Yao, J. H. Xu, J. J. Fu, Extremely strengthening fatigue resistance, elastic restorability and thermodynamic stability of a soft transparent self-healing network based on a dynamic molecular confinement-induced bioinspired nanostructure. *Mater. Horiz.* **10**, 2968–2979 (2023).
18. R. Chen, J. Shi, T. Zhao, S. Li, H. Wang, J. Xu, B. Guo, F. Zhou, Swelling induced hardening and degradation induced slow-expansion hydrogel for a modified cervical spinal cord compression animal model. *ACS Appl. Mater. Interfaces* **16**, 58274–58285 (2024).
19. D. Xiang, L. Liu, Y. Liang, Effect of hard segment content on structure, dielectric and mechanical properties of hydroxyl-terminated butadiene-acrylonitrile copolymer-based polyurethane elastomers. *Polymer* **132**, 180–187 (2017).
20. X. Yan, K. Yang, B. Song, L. Li, L. Han, R. Zhang, Polyurethane with long hard segment for self-healing in blood environment around body temperature. *Chem. Eng. J.* **487**, 150509 (2024).
21. Y. Chen, Z. Tang, Y. Liu, S. Wu, B. Guo, Mechanically robust, self-healable, and reprocessable elastomers enabled by dynamic dual cross-links. *Macromolecules* **52**, 3805–3812 (2019).
22. R. Guo, Q. Zhang, Y. Wu, H. Chen, Y. Liu, J. Wang, X. Duan, Q. Chen, Z. Ge, Y. Zhang, Extremely strong and tough biodegradable poly(urethane) elastomers with unprecedented crack tolerance via hierarchical hydrogen-bonding interactions. *Adv. Mater.* **35**, 2212130 (2023).
23. W. Li, H. Wu, Y. Huang, Y. Yao, Y. Hou, Q. Teng, M. Cai, J. Wu, Ultra-fast-healing glassy hyperbranched plastics capable of restoring 26.4 mpa tensile strength within one minute at room temperature. *Angew. Chem. Int. Ed. Engl.* **63**, e202408250 (2024).
24. H. Wu, H. Wang, M. Luo, Z. Yuan, Y. Chen, B. Jin, W. Wu, B. Ye, H. Zhang, J. Wu, Mechanically robust, self-reporting and healable polyurethane elastomers by incorporating symmetric/asymmetric chain extenders. *Mater. Horiz.* **11**, 1548–1559 (2024).
25. H. Xiong, H. Wu, J. Zhang, S. Huang, S. Gu, Y. Hou, Q. Wu, J. Wu, Healable and recyclable polyurethane with natural-rubber-like resilience via π-type tweezer structure stabilizing dynamical hard domains. *Macromolecules* **56**, 8581–8591 (2023).
26. J. Shi, T. Zheng, J. Yuan, C. Qiu, Y. Ha, H. Zhang, B. Guo, J. Xu, Designing a self-healing shape memory polymer with high stiffness and toughness: The role of nonuniform chain networks. *Macromolecules* **57**, 10987–10995 (2024).
27. S. Keten, Z. Xu, B. Ihle, M. J. Buehler, Nanoconfinement controls stiffness, strength and mechanical toughness of β-sheet crystals in silk. *Nat. Mater.* **9**, 359–367 (2010).
28. I. Agnarsson, M. Kuntner, T. A. Blackledge, Bioprospecting finds the toughest biological material: Extraordinary silk from a giant riverine orb spider. *PLOS ONE* **5**, e11234 (2010).
29. S. M. Lee, E. Pippel, U. Gösele, C. Dresbach, Y. Qin, C. V. Chandran, T. Bräuniger, G. Hause, M. Knez, Greatly increased toughness of infiltrated spider silk. *Science* **324**, 488–492 (2009).
30. T. Guan, X. Wang, Y. L. Zhu, L. Qian, Z. Lu, Y. Men, J. Li, Y. Wang, J. Sun, Mechanically robust skin-like poly(urethane-urea) elastomers cross-linked with hydrogen-bond arrays and their application as high-performance ultrastretchable conductors. *Macromolecules* **55**, 5816–5825 (2022).
31. C. Liu, N. Morimoto, L. Jiang, S. Kawahara, T. Noritomi, H. Yokoyama, K. Mayumi, K. Ito, Tough hydrogels with rapid self-reinforcement. *Science* **372**, 1078–1081 (2021).

32. T. Fujiyabu, N. Sakumichi, T. Katashima, C. Liu, K. Mayumi, U.-I. Chung, T. Sakai, Tri-branched gels: Rubbery materials with the lowest branching factor approach the ideal elastic limit. *Sci. Adv.* **8**, eabk0010 (2022).
33. X. Guo, J. Liang, Z. Wang, J. Qin, Q. Zhang, S. Zhu, K. Zhang, H. Zhu, Tough, recyclable, and degradable elastomers for potential biomedical applications. *Adv. Mater.* **35**, e2210092 (2023).
34. Z. Li, Y. L. Zhu, W. Niu, X. Yang, Z. Jiang, Z. Y. Lu, X. Liu, J. Sun, Healable and recyclable elastomers with record-high mechanical robustness, unprecedented crack tolerance, and superhigh elastic restorability. *Adv. Mater.* **33**, 2101498 (2021).
35. S. R. Petersen, H. Prydderch, J. C. Worch, C. J. Stubbs, Z. Wang, J. Yu, M. C. Arno, A. V. Dobrynin, M. L. Becker, A. P. Dove, Ultra-tough elastomers from stereochemistry-directed hydrogen bonding in isosorbide-based polymers. *Angew. Chem. Int. Ed. Engl.* **61**, e202115904 (2022).
36. Z. Guo, X. Lu, X. Wang, X. Li, J. Li, J. Sun, Engineering of chain rigidity and hydrogen bond cross-linking toward ultra-strong, healable, recyclable, and water-resistant elastomers. *Adv. Mater.* **35**, 2300286 (2023).
37. X. Zhu, W. Zhang, G. Lu, H. Zhao, L. Wang, Ultrahigh mechanical strength and robust room-temperature self-healing properties of a polyurethane-graphene oxide network resulting from multiple dynamic bonds. *ACS Nano* **16**, 16724–16735 (2022).
38. M. Li, L. Chen, Y. Li, X. Dai, Z. Jin, Y. Zhang, W. Feng, L. T. Yan, Y. Cao, C. Wang, Superstretchable, yet stiff, fatigue-resistant ligament-like elastomers. *Nat. Commun.* **13**, 2279 (2022).
39. W. Yang, Y. Zhu, T. Liu, D. Puglia, J. M. Kenny, P. Xu, R. Zhang, P. Ma, Multiple structure reconstruction by dual dynamic crosslinking strategy inducing self-reinforcing and toughening the polyurethane/nanocellulose elastomers. *Adv. Funct. Mater.* **33**, 2213294 (2023).
40. X. Wang, J. Sun, Engineering of reversibly cross-linked elastomers toward flexible and recyclable elastomer / carbon fiber composites with extraordinary tearing resistance. *Adv. Mater.* **36**, e2406252 (2024).
41. Z. Fang, H. Mu, Z. Sun, K. Zhang, A. Zhang, J. Chen, N. Zheng, Q. Zhao, X. Yang, F. Liu, J. Wu, T. Xie, 3D printable elastomers with exceptional strength and toughness. *Nature* **631**, 783–788 (2024).
42. C. Chu, W. Sun, S. Chen, Y. Jia, Y. Ni, S. Wang, Y. Han, H. Zuo, H. Chen, Z. You, M. Zhu, Squid-inspired anti-salt skin-like elastomers with superhigh damage resistance for aquatic soft robots. *Adv. Mater.* **36**, e2406480 (2024).
43. Z. Zhang, C. Lin, R. Hou, D. Tang, Construction of polyallophanate vitrimers from poly(urea carbonate) via group revival induced crosslinking. *Eur. Polym. J.* **161**, 110819 (2021).
44. X. Wang, Y. I. Wang, X. Yang, Z. Lu, Y. Men, J. Sun, Skin-inspired healable conductive elastomers with exceptional strain-adaptive stiffening and damage tolerance. *Macromolecules* **54**, 10767–10775 (2021).
45. C. M. Hartquist, S. Lin, J. H. Zhang, S. Wang, M. Rubinstein, X. Zhao, An elastomer with ultrahigh strain-induced crystallization. *Sci. Adv.* **9**, eadj0411 (2023).
46. L. Wang, L. Guo, K. Zhang, Y. Xia, J. Hao, X. Wang, Development of tough thermoplastic elastomers by leveraging rigid–flexible supramolecular segment interplays. *Angew. Chem. Int. Ed. Engl.* **62**, e202301792 (2023).
47. L. Wang, K. Zhang, X. Zhang, Y. Tan, L. Guo, Y. Xia, X. Wang, Mismatched supramolecular interactions facilitate the reprocessing of super-strong and ultratough thermoset elastomers. *Adv. Mater.* **36**, e2311758 (2024).
48. J. Xu, Y. Li, T. Liu, D. Wang, F. Sun, P. Hu, L. Wang, J. Chen, X. Wang, B. Yao, J. Fu, Room-temperature self-healing soft composite network with unprecedented crack propagation resistance enabled by a supramolecular assembled lamellar structure. *Adv. Mater.* **35**, e2300937 (2023).
49. D. Wang, Z. Wang, S. Ren, J. Xu, C. Wang, P. Hu, J. Fu, Molecular engineering of a colorless, extremely tough, superiorly self-recoverable, and healable poly(urethane-urea) elastomer for impact-resistant applications. *Mater. Horiz.* **8**, 2238–2250 (2021).
50. J. Xu, M. Shao, X. Wang, T. Chen, S. Li, X. Zhang, T. Wang, Y. Zhang, Z. Yang, Q. Wang, Flexible cages enable robust supramolecular elastomers. *Adv. Mater.* **36**, e2311992 (2024).
51. S. Lin, X. Zhao, Fracture of polymer networks with diverse topological defects. *Phys. Rev. E* **102**, 052503 (2020).
52. R. P. Wool, K. M. O'Connor, A theory crack healing in polymers. *J. Appl. Phys.* **52**, 5953–5963 (1981).
53. G. M. Scheutz, J. J. Lessard, M. B. Sims, B. S. Sumerlin, Adaptable crosslinks in polymeric materials: Resolving the intersection of thermoplastics and thermosets. *J. Am. Chem. Soc.* **141**, 16181–16196 (2019).
54. J. Shi, T. Zheng, Z. Wang, P. Wang, H. Yang, J. Guo, D. Wang, B. Guo, J. Xu, Filler effects inspired high performance polyurethane elastomer design: Segment arrangement control. *Mater. Horiz.* **11**, 4747–4758 (2024).
55. W. He, D. Zhou, H. Gu, R. Qu, C. Cui, Y. Zhou, Y. Wang, X. Zhang, Q. Wang, T. Wang, Y. Zhang, A biocompatible 4d printing shape memory polymer as emerging strategy for fabrication of deployable medical devices. *Macromol. Rapid Commun.* **44**, e2200553 (2023).
56. Z. Dong, X. Ren, B. Jia, X. Zhang, X. Wan, Y. Wu, H. Huang, Composite patch with negative Poisson's ratio mimicking cardiac mechanical properties: Design, experiment and simulation. *Mater. Today Bio* **26**, 101098 (2024).
57. Y. Jiang, K. Shi, L. Zhou, M. He, C. Zhu, J. Wang, J. Li, Y. Li, L. Liu, D. Sun, G. Feng, Y. Yi, L. Zhang, 3D-printed auxetic-structured intervertebral disc implant for potential treatment of lumbar herniated disc. *Bioact. Mater.* **20**, 528–538 (2023).
58. O. K. Baskurt, H. J. Meiselman, Erythrocyte aggregation: Basic aspects and clinical importance. *Clin. Hemorheol. Microcirc.* **53**, 23–37 (2013).
59. J. A. Reid, A. McDonald, A. Callanan, Modulating electrospun polycaprolactone scaffold morphology and composition to alter endothelial cell proliferation and angiogenic gene response. *PLOS ONE* **15**, e0240332 (2020).
60. Y. Li, X. Li, R. Zhao, C. Wang, F. Qiu, B. Sun, H. Ji, J. Qiu, C. Wang, Enhanced adhesion and proliferation of human umbilical vein endothelial cells on conductive PANI-PCL fiber scaffold by electrical stimulation. *Mater. Sci. Eng. C* **72**, 106–112 (2017).

Acknowledgments

Funding: This work was supported by the National Natural Science Foundation of China 52403011 (to J.S.), 82204322 (to C.Q.), and 82373821 (to C.Q.), the Fundamental Research Funds for the Scientific and Technological Innovation Project of China Academy of Chinese Medical Sciences CI2023E002 (to C.Q.) and CI2023E005TS02 (C.Q.), and the Beijing Nova Program 20240484502 (to C.Q.). **Author contributions:** Conceptualization: J.S., J.X., and C.Q. Methodology: J.S. and C.Q. Validation: J.S., F.X., Q.T., and C.W. Formal analysis: J.S., F.X., Q.T., and C.W. Investigation: J.S., F.X., Q.T., C.W., and B.L. Resources: J.X., B.G., J.S., and C.Q. Data curation: J.S. and C.Q. Writing—original draft: J.S. and C.Q. Writing—review and editing: J.X., J.S., and C.Q. Visualization: J.S., Z.W., and C.Q. Supervision: J.X., B.G., and C.Q. Project administration: J.X., J.S., and C.Q. Funding acquisition: J.X., B.G., C.Q., and J.S. **Competing interests:** J.X., J.S., and B.G. are the inventors on a patent application related to this work filed by Tsinghua University (serial no. 2023080216, dated 08 March 2024). The authors declare that they have no other competing interests. **Data and materials availability:** All data needed to evaluate the conclusions in the paper are present in the paper and/or the Supplementary Materials. All animal studies were approved by the Institutional Animal Care and Use Committee and Animal Ethics Committee of the Institute of Chinese Materia Medica (no. 2024B220).

Submitted 20 December 2024
Accepted 8 May 2025
Published 13 June 2025
10.1126/sciadv.adv4646